Article

InP/ZnS Quantum Dots for High-Sensitivity Temperature Sensors

Barnali Mahato, Palash Kusum Das, and Asha Bhardwaj*

Read Online

ACCESS | 📊 Metrics & More | 📖 Article Recommendations | 🆘 Supporting Information

ABSTRACT: In this work, we report the synthesis of high-quality, nontoxic InP/ZnS core−shell quantum dots (QDs). The temperature-dependent optical properties such as photoluminescence (PL), absorption, and PL decay with time have been investigated. Based on the temperature dependence of optical properties of QDs, three different configurations of temperature sensors using PMMA as the QD host material were fabricated. The temperature sensor configurations are planar thin-film (InP/ZnS QD)/PMMA deposited on a Si wafer (sensor 1), (InP/ZnS QD)/PMMA-filled borosilicate fibers (sensor 2), and InP/ZnS QD-doped electrospun PMMA nanofibers deposited on a Si wafer (sensor 3). After fabrication, the performance of the temperature sensors have been thoroughly investigated through photoluminescence reversibility tests in consecutive heating−cooling cycles, and the sensitivity of the sensors has been calculated. The three sensors have shown different critical reversible temperatures above which they go through irreversible structural damage and lose their reversibility. The highest critical reversible temperature of 95 °C and the highest sensitivity of 2.1% °C^{-1} have been achieved, which are comparable to Cd- and dye-based temperature sensors reported to date. The sensors were found to be highly stable, which demonstrated negligible degradation even after 30 days of exposure to ambient conditions. The InP/ZnS QD-based optical temperature sensors can be considered to be a potential replacement for toxic heavy-metal QD-based optical temperature sensors.
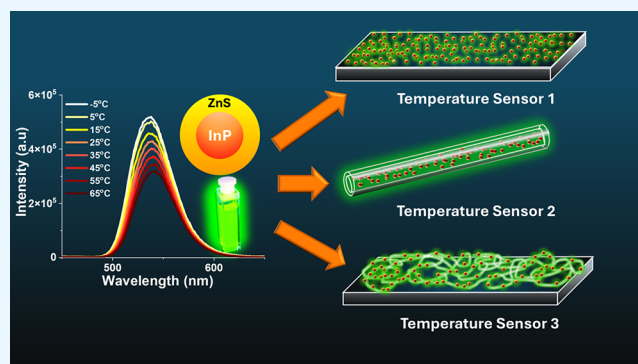
1. INTRODUCTION

Semiconductor quantum dots (SQDs) are highly promising nanomaterials in optoelectronics, quantum communication, and medical science domains.[1−3] Compared to traditional organic fluorophores, SQDs offer a variety of advantages such as precisely tunable photoemission, tunable photoexcitation due to the broad absorption range, and remarkable resistance against photobleaching.[4] Majority of conventional QDs are based on poisonous heavy-metal ions such as Cd and Pb, which are detrimental to the environment as well as human health. Therefore, nontoxic InP-based QDs, which show similar optical performance, appear to be potential alternatives for the toxic heavy-metal ion-based QDs.[5]

In recent years, because of 3D carrier confinement, quantum dot (QD) systems have garnered significant attention for application in high-performance optoelectronic devices.[6,7] Nevertheless, a major issue that QD devices have yet to overcome is their degraded function at high temperatures.[8] The temperature-dependent photoluminescence properties of quantum dots (QDs) hold significant importance for QD-based optoelectronic devices, including photovoltaic systems, light concentrators, and light-emitting diodes (LEDs).[9,10] Even at high temperatures, these functional devices should remain steady and operate with high efficiency. Thus, it is imperative to understand and optimize the temperature dependence of optical characteristics of QDs.[11−13]

On the other hand, luminescence thermometry is a versatile optical technique that uses temperature-dependent variation in luminescence characteristics (e.g., excited-state lifetime, emission intensity etc.) as an indicator or probe to determine the local temperature.[14] Optical temperature sensors have so far been employed using a broad variety of luminescent materials, such as organic dyes,[15] inorganic phosphors,[14] and luminescent coordination complexes.[16] QDs outperform these luminous materials in terms of PL intensity, narrow full width at half-maxima (fwhm), and multiparameter detectable signals. However, until now, the available optical temperature sensors are mostly based on toxic Cd-based QDs. Nonetheless, there are still a number of issues with QD-based optical temperature probes that need to be addressed. Previously developed CdSe-based solid-state optical temperature sensors show poor responsivity, low thermal stability, and a narrow working
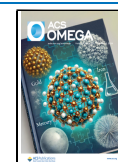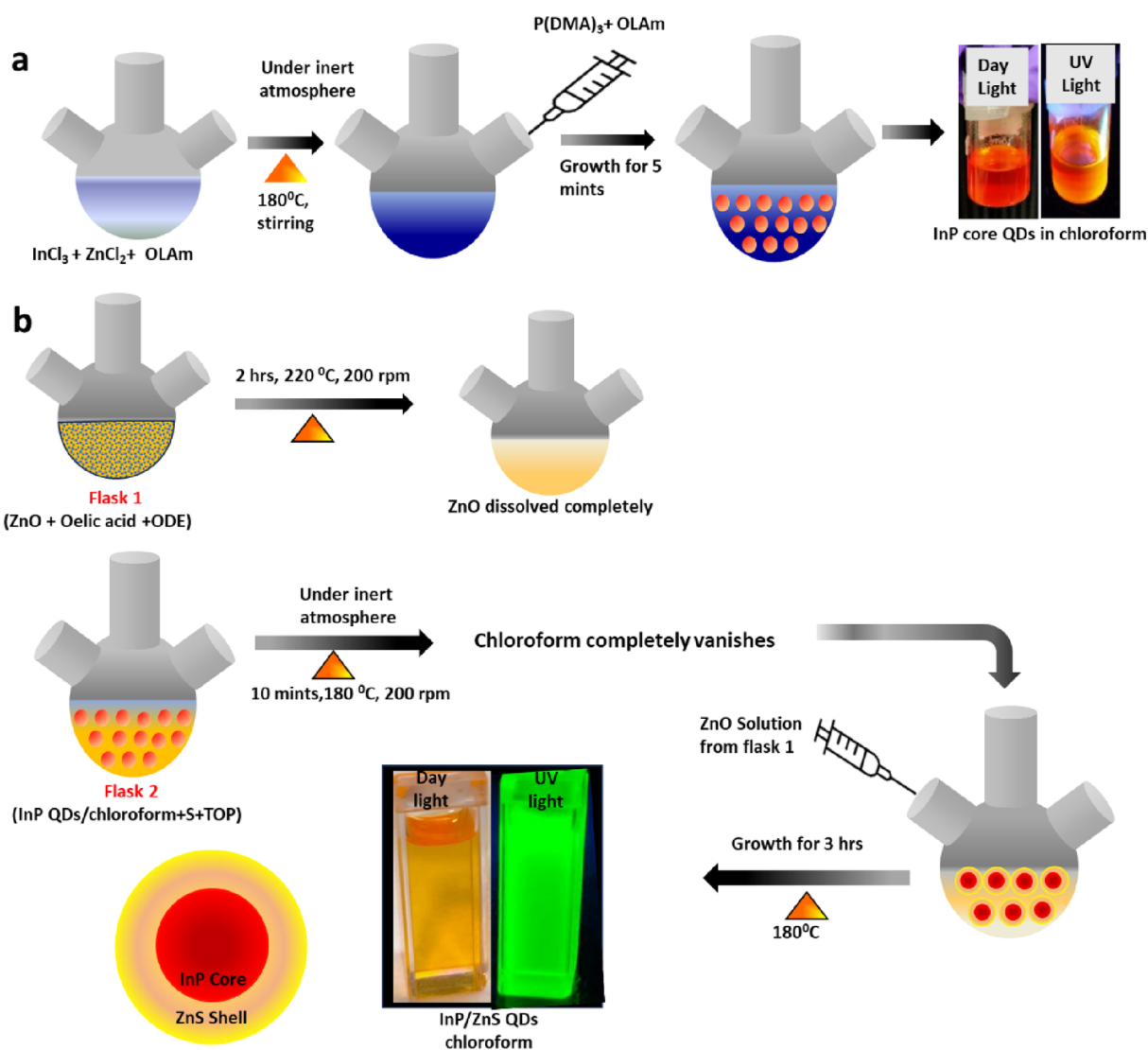
Figure 1. Schematic of the synthesis procedure of (a) InP and (b) InP/ZnS core−shell quantum dots.

temperature range.[17−20] Apart from these drawbacks, the toxicity concerns due to the presence of heavy-metal ions (Cd, Pb, etc.) remain a threat to the environment as well as human health. It is therefore still a challenging task to fabricate nontoxic QD-based optical temperature sensors with high sensitivity, stability, and repeatability.

However, InP-based QDs appear to be nontoxic and therefore a potential replacement for Cd-based QDs. Although several studies have been done on the temperature-dependent optical properties of nontoxic InP-based QDs,[21−26] temperature sensor fabrication and detailed analysis of their performance are still not reported. The PL characteristics of InP/ZnS core/shell QDs were examined by Narayanaswamy et al. in 2008 for temperatures ranging from 300 to 525 K.[21] When the temperature was increased for these QDs, a narrowing of the band gap and a broadening of the PL line width were observed, which were attributed to enhanced interactions between excitons and phonons. In 2009, the same group demonstrated the temperature-dependent PL characteristics of InP/ZnS QDs ranging from 2 to 525 K,[22] and the observed change in both the PL peak and line width was attributed to scattering from acoustic phonons. The PL intensity of InP and InP/ZnS QDs at temperatures ranging from 300 to 800 K was compared by

Rowland et al. in 2014.[23] They reported a decrease in PL intensity on increase in temperature, which was explained by the trapping of electrons in the surface trap states. Further, Shirazi et al. in 2012 examined the PL characteristics of InP/ZnS QDs for temperature ranging from room temperature to liquid helium temperature. They observed multiexponential exciton decay curves, which were well-explained by the presence of bright and dark exciton states, as well as defect states.[24] Later, a couple of groups carried out a low-temperature PL variation study on InP/ZnS QDs and found that the occurrence of nonradiative channels with an increasing temperature is the reason for PL intensity attenuation. The interaction between excitons and longitudinal acoustic (LA) phonons was identified as the cause of the redshift in PL spectra.[25] The presence of fast and slow PL decay components and their change with increasing temperature were well-explained by the fine structure of excitons.[26] In 2020, another study by Wang et al. investigated the temperature-dependent PL properties of InP/ZnS QDs and explained the exciton−phonon coupling in detail.[27] In 2022, our group has reported a study on InP/ZnS QD-based temperature sensors where only a thin-film-based planar-configuration temperature sensor was reported.[28] Although the reported work on InP/ZnS is encouraging, all the previous studies were focused on

investigating the change in PL intensity, PL peak wavelength shift, and line width broadening with temperature. Various theories on the temperature-dependent optical properties of InP/ZnS QDs were put forward, but the fabrication of temperature sensors and the investigation of their performance are still not available.

In this work, we report a comprehensive study of InP/ZnS QD-based temperature sensors. First, the synthesis of InP core QDs and then InP core QDs shelled with a higher-band-gap material ZnS for better confinement of charge carriers and passivation of core surface trap states was carried out. Further, the temperature dependence of absorption, PL intensity, PL fwhm, peak position, and decay time of InP/ZnS QDs was investigated. For enhancing the thermal stability, optical transparency, and chemical inertness, poly(methyl methacrylate) (PMMA) was chosen as a host material for QD encapsulation. By providing a protective and stable environment for the quantum dots, PMMA helps ensure the reliable performance and longevity of the temperature sensors under varying temperatures. Finally, based on PMMA-encapsulated InP/ZnS QDs, three distinct temperature sensors were fabricated: a QD/PMMA thin-film-based planar configuration, QD/PMMA-filled borosilicate fibers, and QD-doped electrospun PMMA nanofibers deposited on a silicon substrate. For a planar-configuration sensor, QD/PMMA was drop cast on a silicon substrate, while a hollow borosilicate capillary was filled with QD/PMMA for QD-containing optical-fiber temperature sensors. For QD-doped electrospun nanofiber configuration, the QD/PMMA composite was used to electrospun polymer nanofibers containing QDs on silicon substrate. Further, the sensors were thoroughly studied for their reversible sensing response in heating–cooling cycles, repeatability, reliability, sensitivity, and stability. A sensitivity as high as 2.1% $°C^{-1}$ was achieved, which is very much comparable to previously reported Cd-based temperature sensors.[29] The stability of the temperature sensors was examined on exposure to ambient conditions for as long as 30 days. The sensors show very little degradation, confirming their reliability and stability.

2. INP/ZNS QD SYNTHESIS AND TEMPERATURE SENSOR FABRICATION

2.1. Synthesis of InP Core QDs. InP QDs were synthesized by using indium(III) chloride ($InCl_3$) and tris(dimethylamino)-phosphine ($P(DMA)_3$) as main precursors through the hot injection method in an inert atmosphere (Figure 1a) using a Schlenk line setup. $InCl_3$ (0.45 mmol), Zn(II) chloride ($ZnCl_2$) (300 mg, 2.2 mmol), and oleyl amine (OLAm) (5.0 mL, 15 mmol) were taken in a 100 mL three-neck flask. OLAm acts as a solvent for the precursors as well as a capping ligand. In addition, $ZnCl_2$ acts as Z-type ligand, where Zn^{2+} activates the phosphorus precursor and promotes the formation of the ZnS shell.[14] The reaction mixture was degassed under vacuum for a minimum of 30 min at 120 °C and 200 rpm constant stirring to remove oxygen and water, if any. Further, the reaction mixture was switched to an argon atmosphere and heated to 180 °C. After 10 min, when $InCl_3$ has dissolved completely and the solution has become clear, tris(dimethylamino)phosphine ($P(DMA)_3$) (0.45 mL, 1.6 mmol) was injected rapidly. The reaction started right after the phosphine precursor ($P(DMA)_3$) injection, and the solution turned bright orangish red, indicating the formation of core-only InP QDs. The InP core growth was allowed for 5 min, after which the flask was cooled down to room temperature naturally, core-only InP QDs were precipitated in

ethanol (50 mL) , centrifuged (5000 rpm), and the precipitate was suspended in an organic solvent (chloroform).

2.2. Synthesis of InP/ZnS Core–Shell QDs. To shell the InP core with ZnS, zinc oxide (ZnO) and sulfur (S) were used as main precursors (Figure 1b). Oleic acid (OA) was used as a surface-capping ligand and 1-octadecene(ODE) as a high-boiling-point noncoordinating solvent. ZnO (0.7 mmol), OA (9 mmol), and ODE (7 mL) were taken in a flask and after degassing for 2 h at 220 °C were heated at 250 °C in an Ar atmosphere for 5 min with constant stirring at 200 rpm. After complete dissolution of ZnO, the solution was injected to another flask containing InP QDs (in chloroform (2 mL)), sulfur (0.7 mmol), and TOP (0.7 mL) in an Ar atmosphere and then heated for 3 h at 180 °C. Before the hot injection of the Zn precursor, the InP QDs- and S precursor-containing flask was heated for 10 min (chloroform evaporated completely in 10 min) at 180 °C and 200 rpm constant stirring in an Ar atmosphere. After completion of the reaction, the solution was cooled down to room temperature, and InP/ZnS QDs were cleaned using ethanol followed by centrifugation (7000 rpm, 10 min). The obtained precipitates were suspended in chloroform.

2.3. Temperature Sensor Device Fabrication and Characterization Set Up. In order to further stabilize the QDs, they were encapsulated in a PMMA polymer. For PMMA/QD composite formation, first, PMMA (1 g) was dissolved in chloroform (6 mL) to form a 10 wt % solution and then stirred for 1 h. Further, 0.5 mL of the InP/ZnS QD solution having a concentration of ∼20 mg/mL was added. The mixture was stirred for another 1 h and ultrasonicated a few times to form the homogeneous polymer QD composite. Henceforth, the following was performed:

- The QD/PMMA solution was drop cast on a silicon wafer to form a planar temperature sensor: sensor 1.
- A hollow borosilicate capillary was filled with the same QD/PMMA composite and left overnight to solidify completely to form a QD core fiber temperature sensor: sensor 2.
- The same composite solution was used to deposit electrospun fibers on a silicon wafer to form a nanofiber temperature sensor: sensor 3.

The schematic of the experimental setup used to investigate the impact of cyclic heating–cooling on the PL properties of QD-based temperature sensors is shown in the Supporting Information (Figure S1).

1. The silicon wafer-based (QD/PMMA drop cast on Si and QD/PMMA electrospun fibers deposited on Si) devices were placed at the top of the heating stage and illuminated by 365 nm UV light (30 W), kept above at a height of 30 cm. The temperature-dependent PL response was collected by a multimode fiber (core diameter of 600 μm, NA = 0.52) and recorded by a portable spectrometer (Ocean Optics, USB2000) by varying the temperature of the heating stage.
2. Similarly, the QD/PMMA composite-filled borosilicate fiber was placed on the hot plate, and the QDs inside were excited by a laser source (CW, 405 nm) from one end. The detector probe was fixed at the other end, and the PL emission was recorded with varying stage temperatures.

3. RESULTS AND DISCUSSION

3.1. InP/ZnS Quantum Dots. *3.1.1. Structural Characterization.* The TEM and HRTEM images (Figure 2a,b) of InP
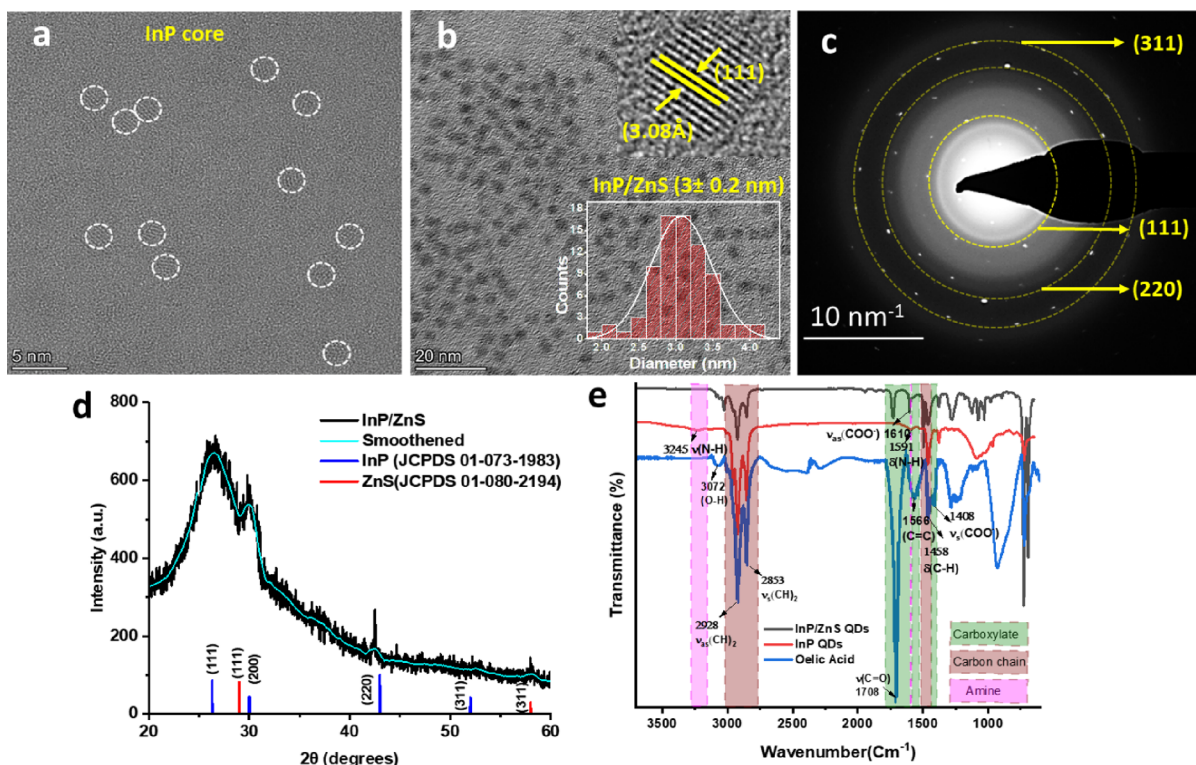
Figure 2. (a) HRTEM image of InP core QDs, (b) TEM image of InP/ZnS QDs with the inset showing the HRTEM image and size distribution histogram. (c) SAED pattern of InP/ZnS QDs, (d) XRD spectra of InP/ZnS QDs, and (e) FTIR spectra of InP and InP/ZnS QDs.
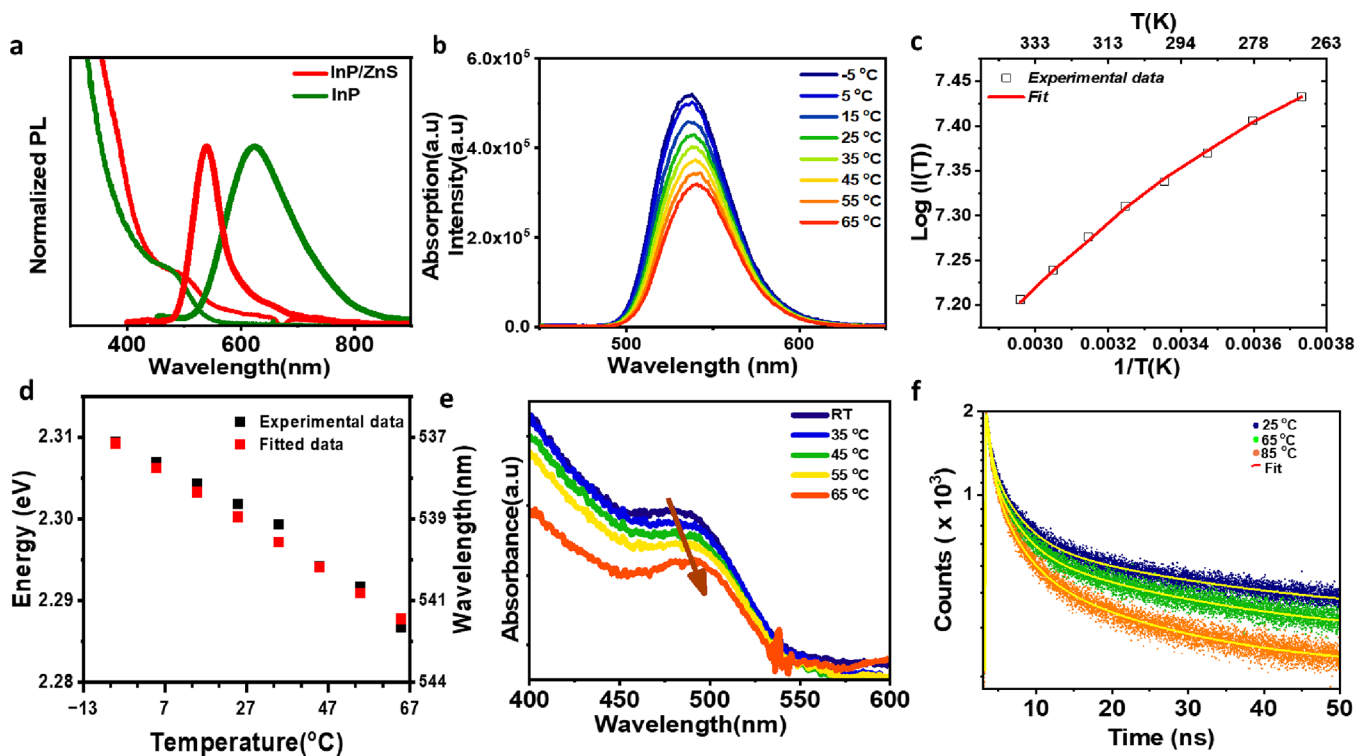

Figure 3. (a) Emission and absorption spectra of synthesized InP and InP/ZnS QDs. (b) Temperature-dependent PL spectra of InP/ZnS QDs. (c) PL intensity variation with temperature in the logarithmic scale. (d) Energy and peak wavelength shift with temperature for InP/ZnS QDs. (e) Absorption spectra variation with temperature. (f) Time-resolved PL decay profile for InP/ZnS QDs from RT to 85 °C.

core and InP/ZnS core−shell QDs show that they are crystalline in nature, spherical in shape and have average diameters of 2 and 3 nm, respectively. InP/ZnS QDs' average size is confirmed from

the histogram of the size distribution and the Gaussian fit (Figure 2b inset). The HRTEM image (Figure 2b inset) of InP/ZnS QDs shows the interplanar spacing of 3.08 Å, which

corresponds to the zinc blend ZnS (111) crystalline plane. The SAED pattern in Figure 2c confirms the highly crystalline nature of InP/ZnS QDs, and the three concentric rings correspond to the (111), (220), and (311) planes. The EDX investigation of InP/ZnS core/shell QDs confirms the presence of phosphorus (P), sulfur (S), zinc (Zn), and indium (In) with atomic percentages of 9, 24, 65, and 2%, respectively (Figure S2).

XRD analysis of the QDs was carried out to further analyze the crystal structure. Figure 2d shows the XRD patterns of InP/ZnS QDs. The observed diffraction peaks at 26.2, 30.4, 43.6, and 53.0° are assigned to the (111), (200), (220), and (311) planes of the InP zinc blende crystalline phase (JCPDS PDF database no. 01-073-1983). Diffraction peaks located at 28.9 and 58.0° are related to the (111) and (311) planes of the ZnS zinc blende crystalline phase (JCPDS PDF database no. 01-080-2194).

The FTIR analysis was done to study the surface passivation of both InP and InP/ZnS QDs. From the FTIR spectra in Figure 2e, it can be seen that both the samples show the presence of symmetric and antisymmetric stretching vibration of CH_2 groups in the range of 2850−2925 cm^{-1}, which suggest that the QDs are capped by long alkyl ligands. The presence of a broad resonance peak at 3230 cm^{-1}, which originates from N−H stretching, suggests that the pristine InP core is covered by amine-related species.[30] The absence of a peak in 3000−3500 cm^{-1} in InP/ZnS core−shell QDs indicates the removal of ligands present on the core InP QD surface. The resonance peaks present at 1603 cm^{-1} in InP/ZnS QDs confirm the COO− stretching of the carboxylate group indicating the presence of the oleic acid (OA) surface ligand. The presence of C=O stretching related to free OA molecules is confirmed by the resonance signal at 1710 cm^{-1}. It can be concluded from FTIR analysis that the amine groups, which were visible in InP QDs, are changed to OA on ZnS shelling.

3.1.2. Optical Characterization. The core−shell structure of InP/ZnS quantum dots plays a crucial role in improving their optical characteristics, stability, quantum confinement, emission wavelength tunability, and control over the Stokes shift. As the band gap of bulk ZnS (3.60 eV) is wider than that of InP (1.34 eV), it is used to shell and passivate the InP core surface and confine the charge carriers. Figure 3a shows the absorption and PL spectra of the as-synthesized InP core and InP/ZnS core−shell QDs. From the absorption spectra, it can be seen that the excitonic absorption peak of InP QDs appears at ∼480 nm, which does not change much after shelling with ZnS, confirming the unaltered confinement of the core charge carriers. As compared to the bulk InP band gap (∼925 nm), the excitonic peaks are significantly blueshifted due to an increase in the quantum confinement in nanosized particles. The InP QDs show an orange emission (Figure 1a) under UV illumination with emission maxima at ∼620 nm, whereas after shelling with ZnS, the QDs show a green emission (Figure 1b) with maxima at ∼540 nm. The blueshift in PL maxima is likely a result of a combination of quantum confinement effects, surface passivation, stress and strain effects, charge transfer processes, and nanocrystal size. These factors collectively contribute to the modification of the nanocrystal electronic structure and optical properties, leading to the observed spectral shift in the luminescence spectrum. As compared to the 1% photoluminescence quantum yield (QY) in InP core QDs, a 31% PLQY was observed for InP/ZnS QDs (which increased further to 42% in the InP/ZnS QD-PMMA composite, Supporting Information Section S(A), Figure S3) with a remarkable

decrease in the full width half-maxima (fwhm) from 130 to 46 nm due to passivation of surface defect states by the ZnS shell.

Further, the temperature dependence of emission characteristics of the QDs was investigated. Figure 3b shows the PL emission of QDs dispersed in chloroform at various temperatures ranging from −5 to 65 °C. The maximum emission intensity was observed to be at −5 °C, which decreased by 38% when the temperature was increased to 65 °C due to activation of trap states and other nonradiative centers with an increase in temperature. In order to understand further, the temperature-dependent PL intensity was plotted and fitted (Figure 3c) with the Mott equation (eq 1) from a conventional model of thermal quenching in solids:[31−33]

$$I(T) = \frac{I(0)}{1 + A\ exp^{-E_a/k_B T}} \tag{1}$$

where $I(T)$ is the PL maximum intensity at temperature T, $I(0)$ is the PL intensity at 0 K, E_a is the activation energy for thermal quenching, A is a pre-exponential factor related to the frequency of nonradiative recombination events, and k_B is the Boltzmann constant. From the fitted data, the activation energy E_a was found to be 15.25 ± 2 meV, which can be attributed to nonradiative relaxation of excitons through corresponding energy bands of surface and defect states.[27] The values of constants A and $I(0)$ were found to be 9.1 ± 0.6 and 4.3 ± 0.2 × 10^7, respectively. Further, the interatomic spacing in QDs also varies as the temperature rises, leading to an increase in lattice strain due to an imbalance in the thermal expansion rates of the core and shell, which further increases trap states and enhances nonradiative recombination of charge carriers. Also, a redshift in the emission peak is observed with an increase in temperature (Figure 3d), which is due to the energy band gap shifting with temperature, which is well-characterized by Varshni's equation (eq 2).

$$E_g(T) = E_g(0) + \frac{\alpha T^2}{\beta + T} \tag{2}$$

where $E_g(T)$ is the band gap at temperature T, $E_g(0)$ is the band gap at $T = 0$ K, α represents the band-gap energy temperature coefficient, and β is a constant, which is of the order of the semiconductor material's Debye temperature. The values of $E_g(0)$, α, and β calculated from this data fitting for InP/ZnS QDs were found to be 2.36 eV, 4.2 ± 0.4 × 10^{-4} eV/K, and 326 ± 58 K, which are a good match with the values reported by Narayanaswamy et al.[21]

Furthermore, temperature-dependent absorption studies were also conducted (Figure 3e). It is found that the excitonic absorption peak shifts to lower energy with an increase in temperature, which is ascribed to expansion of the lattice, thermal expansion imbalance of the core and shell material, mechanical strain, and electron−phonon coupling.[34,35] Also, it is found that the optical density of the excitonic absorption peak in the absorption spectra decreases with an increase in temperature, which can be ascribed to enhanced coupling of ground-state charge carriers with phonons at higher temperatures, thus reducing the chances for occupation of higher energy states by charge carriers.

To further understand the phenomena involved in PL, a temperature-dependent PL lifetime was measured for InP/ZnS QDs (Figure 3f). The PL decay was fitted with a triexponential curve, with the χ^2 value close to 1 (eq 3),
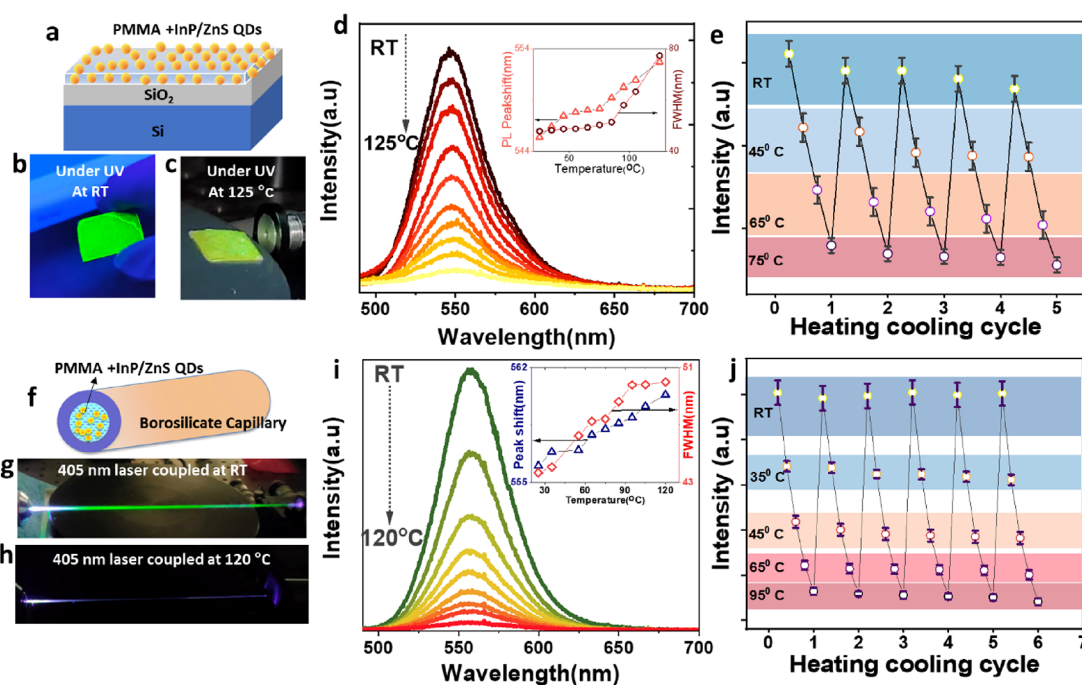
Figure 4. (a) Schematic of the planar thin-film configuration temperature sensor. (b) Planar sensor under UV light at room temperature and (c) under UV light at 125 °C. (d) Temperature-dependent PL spectra; the inset shows the variation of the PL peak shift and fwhm with temperature. (e) Heating−cooling cyclic measurement. (f) Schematic of the QD-filled fiber temperature sensor (g) under laser excitation at RT (h) and under laser excitation at 120 °C. (i) Temperature-dependent PL spectra with variation of the PL peak shift and the fwhm change with temperature in the inset. (j) Heating−cooling cyclic measurement.

$$I(t) = A_o + \sum_{i=1}^{3} A_i\, e^{-t/\tau_i} \tag{3}$$

and can be well-understood from the perspective of thermal activation between "dark" and "bright" states. The band-edge exciton fine-structure splitting is often analyzed by taking into consideration the bright and dark states, which are well-separated by energy spacing Δ with the long-lived dark ground state lying below the short-lived bright state. When $k_BT < \Delta$, excitons are trapped in the dark state, which has a longer lifetime. The exciton's lifetime will shorten when the temperature rises to $k_BT > \Delta$ due to thermal activation of the charge carriers to the short-lived bright state. With a further increment in temperature, the decay time will remain constant when bright- and dark-state populations reach equilibrium. The Δ value of the particular QD is the deciding factor whether the decrease in PL decay time will be observed at a lower temperature or at a higher temperature range. QDs having higher Δ values need higher temperatures to achieve the thermal equilibrium in the carrier population between bright and dark states.[36−41] For InP/ZnS QDs, the three exponentially fitted values are shown in Table S1. The first two lifetimes (τ_1 and τ_2) could be explained with three thermally mixed fine-structure state luminescence models.[42−45] The fast decay τ_3 (<1 ns, close to our Instrument Response function), which remains almost constant with temperature, could be attributed to trapping states. It can be noticed that in the temperature span from 25 to 65 °C, there is a slight decrease in the lifetime value as compared to the range from 65 to 85 °C where the decay is very rapid. Therefore, it can be concluded that the PL lifetime decay in the lower temperature range is due to the redistribution of carriers in dark and bright states in thermal equilibrium. However, the rapid decrease in the PL decay time at higher temperatures indicates additional thermal

quenching that causes structural damage and hence nonradiative surface trap states.[46]

3.2. Temperature Sensors. *3.2.1. Sensor 1: The Thin-Film-Based Planar-Configuration Temperature Sensor.* The InP/ZnS QD-PMMA polymer composite was drop casted on a 10 mm × 10 mm Si (0.5 mm)/SiO$_2$ (0.5 μm) wafer. Figure 4a shows the schematic of the planar device, and Figure 4b,c shows the device under UV light at room temperature and at 125 °C. The emission intensity from the device decreases with the increase in temperature from 25 to 125 °C when illuminated with 365 nm UV light (Figure 4d). Although there is very little chance of host material evaporation in PMMA matrices, PMMA films typically develop surface cracks at very high temperatures.[47] This allows QDs to be exposed to the open atmosphere during heating, which in turn causes photo-oxidation of QDs and the emergence of nonradiative relaxation pathways. For temperatures >125 °C, the signal is too weak to be used for analysis and undergoes irreversible damage due to photo-oxidation. With the increase in temperature from 25 to 125 °C, the fwhm of the emission peak is observed to be widened from 43 to 80 nm (Figure 4d inset). Moreover, a redshift of 0.1 nm/°C in the peak position from 544 to 554 nm with variation in temperature (inset of Figure 4d) from 25 to 125 °C is observed. Figure 4e depicts the reversible response of fluorescence spectra in four consecutive heating−cooling cycles. The highest temperature recorded was 75 °C, and the lowest was 25 °C. Beyond 75 °C (reversible critical temperature), the temperature sensor lost its reversible property due to irreversible degradation of the QDs.

3.2.2. Sensor 2: The InP/ZnS QD-PMMA-Filled Fiber Temperature Sensor. InP/ZnS QD-PMMA-filled borosilicate capillary (110 μm/180 μm) of 60 cm length was used as another configuration to be used as a temperature sensor. In a planar
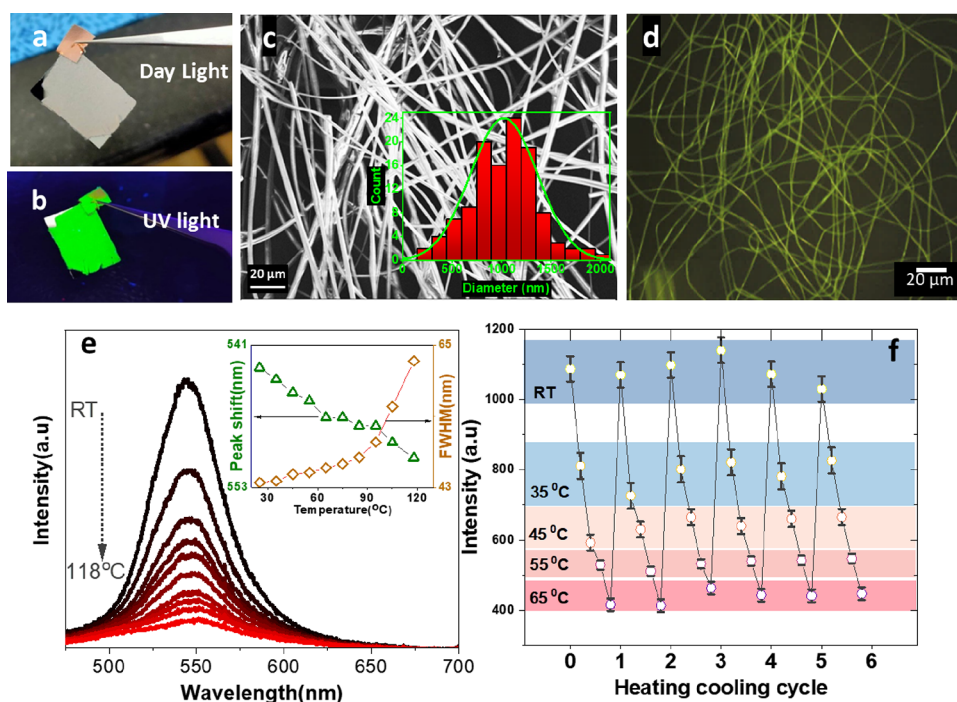
Figure 5. QD-doped electrospun nanofibers deposited on a silicon wafer under (a) daylight and (b) UV light. (c) SEM image. Inset: fiber diameter size distribution histogram. (d) Fluorescence microscope image of the electrospun fibers. (e) Temperature-dependent PL spectra of the fibers on a wafer device, Inset shows the PL peak shift and change in fwhm with temperature. (f) Heating−cooling cyclic reversibility measurement of PL intensity.

configuration, temperature measurement systems have very little immunity from nearby EM interference and stray radiation, which is very well taken care of in fiber-based temperature sensors. Such sensors could find application in various remote and hazardous environments. Figure 4f shows the schematic of the QD-filled fiber, and Figure 4g−h shows the images of the fiber when coupled to a 405 nm CW laser at room temperature and at 120 °C. The emission collected from the fiber peaks at ∼550 nm, which shows that the fiber has a guiding property due to the higher refractive index of the QD/PMMA core as compared to borosilicate cladding. Further, emission spectra were recorded on exposure of the fiber to temperatures ranging from 25 to 120 °C (Figure 4i). The emission intensity decreases with an increase in temperature from RT to 120 °C. For $T > 120$ °C, the emission intensity was insufficient for analysis. The PL emission is redshifted with temperature by 0.05 nm/°C (inset of Figure 4i). The fwhm is observed to increase linearly with temperature from 44 nm (at RT) to 51 nm (at 120 °C) (inset of Figure 4i). The QD-filled fiber has the reversible critical temperature of 95 °C, and its reversibility has been shown up to 5 cycles (Figure 4j). Although the wafer sustains a higher temperature (125 °C) than the fiber (120 °C), the fiber performs better in terms of the reversible critical temperature for the PL response during the heating−cooling cycles. This is due to the fiber cladding's inherent shielding of the QD-containing core, which leaves very little surface area for the QDs to interact with the outer environment, thus enhancing their temperature sustaining ability.

3.2.3. Sensor 3: The QD-Doped Electrospun Nanofiber Temperature Sensor. As an alternative design for temperature sensor devices, QD-doped electrospun nanofibers deposited on a silicon wafer were chosen. It has already been reported that electrospun nanofibers have potential in the fabrication of sensing devices because they have a high surface area, which ultimately enhances their sensitivity.[48−50] Initial reports suggest

that the sensing abilities of the electrospun nanofiber scaffolds used for the detection of a nitro compound DNT, mercury ions $(Hg(II))$, and ferric ions $(Fe(III))$ were many times higher in magnitude than the traditional thin films.[51] Electrospun nanofibers, which typically have a high surface area-to-volume ratio, can enhance the interaction between the quantum dots and the surrounding environment. This increased surface area may lead to improved sensitivity by allowing for more efficient sensing of optical signals, which motivated us to explore these electrospun nanofiber-based temperature sensors. Figure 5a,b shows the image of the device under daylight and UV light. As observed in planar and fiber configurations, the nanofiber-based device also emits green under UV illumination.

The optical microscopy image indicates successful formation of nanofibers (Figure S4). The SEM image of the fibers reveals that the deposited fibers are not very homogeneous in size and possess an average diameter of ∼970 nm (Figure 5c and inset). The fluorescence microscopy images (Figure 5d) reveal that the QDs are successfully and efficiently loaded in the nanofibers, as they exhibit a strong green fluorescence. More details about the electrospinning parameters and detailed methodologies are given in Section S(B), Figure S5 of the Supporting Information. After successful deposition of fibers on a Si wafer, temperature-dependent PL measurements were carried out (Figure 5e) in the temperature range of 25−118 °C. The PL peak position has not significantly shifted on an increase in temperature. A PL peak shift of 0.08 nm/°C and an fwhm change from 43 to 60 nm have been observed (Figure 5e inset). The critical reversible temperature for this configuration of the temperature sensor is 65 °C, and reversibility in PL has been shown here up to 5 cycles (Figure 5f).

Sensitivity is an essential parameter to assess the performance of a sensor. The sensitivity discussed in this article and commonly used in the literature is quantified according to eq 4:[52,53]
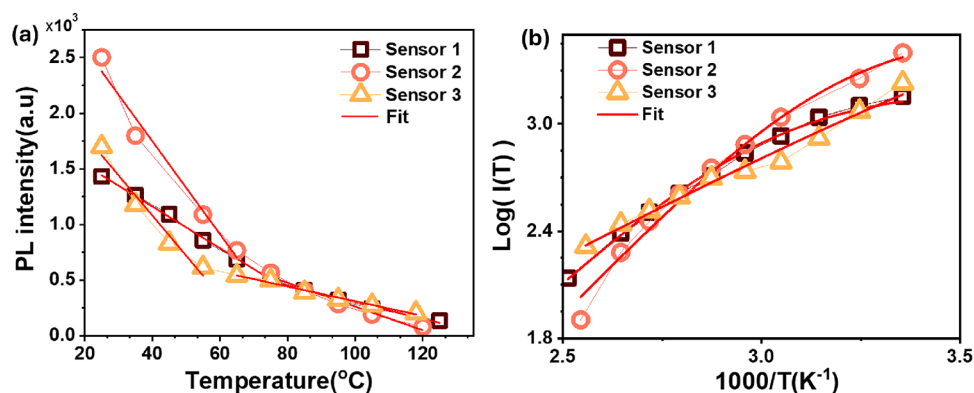
Figure 6. (a) PL intensity variation with temperature for the three temperature sensors. (b) PL intensity variation with temperature in the logarithmic scale.

$$S = \frac{\Delta I}{I(0)\Delta T} \times 100\% \tag{4}$$

where S is sensitivity $[\% \ °C^{-1}]$, $I(0)$ is the intensity at low temperatures, and ΔI is the intensity over a temperature span ΔT. In order to have a comparative study of the fabricated sensors, PL intensity versus temperature has been plotted (Figure 6a) for the three sensors. It can be seen that the decrease in intensity with the increase in the temperature is nonlinear. After 65 °C, the decrease in the PL intensity is almost similar for the three sensors. So, ideally, two working temperature ranges have been chosen, i.e., from RT to 65 and 65 to 120 °C, where the decrease in PL intensity is linear. $\Delta I/\Delta T$ values have been extracted from these two regions by linear fitting, and sensitivity has been calculated. The values are tabulated in Table 1.

Table 1. Sensitivity of the Sensors (Planar, Fibers, Electrospun Nanofibers) in Different Temperature Ranges

sensor configuration	RT−55 °C			60−120 °C		
	$\Delta I/\Delta T$	$I(0)$	S (% °C^{-1})	$\Delta I/\Delta T$	$I(0)$	S (% °C^{-1})
sensor 1: (InP/ZnS QDs)/PMMA/Si wafer	19	1432	1.32	7.4	689	1.07
sensor 2: (InP/ZnS QDs)/PMMA/ borosilicate fiber	41.7	2502	1.6	10.6	767	1.38
sensor 3: (InP/ZnS QDs)/PMMA nanofiber/Si wafer	15.51	1410	1.1	10.88	544	2.1

It can be seen that the temperature sensitivity is higher for the borosilicate fiber-based sensor for lower operating temperatures. At the higher temperature range, the electrospun fibers deposited on the wafer show higher sensitivity than the other two configurations. This is because the packing fraction of the deposited fibers and hence the QDs are very high for electrospun fiber-based temperature sensors, which facilitate efficient interparticle heat transfer. However, to discuss the physical phenomena associated with the decrease in PL intensity with temperature, the Mott equation (eq 1) was fitted (Figure 6b). It is found that the activation energy for thermal quenching is lowest for nanofibers and is the highest for optical fibers. This is because QD-filled fibers have the lowest interaction with the heating environment, while the nanofibers have the highest.

In order to check the long-term stability and repeatability, the devices were stored under ambient conditions in closed containers at room temperature and monitored for 30 days after fabrication. Their performance over multiple heating and cooling cycles, i.e., the reversibility of fluorescence intensity in consecutive heating−cooling cycles, has been investigated for 30 days after sample preparation (Figure 7). It is observed that the behavior of sensor 2 (QD-PMMA-filled borosilicate fiber temperature sensor) remained unaltered after 30 days. For sensors 1 (thin-film-based planar configuration) and 3 (electrospun nanofibers on Si), a decrease in intensity was observed. The measurements were compared for the highest critical reversible temperature and room temperature for each sensor. The stability of sensors is also corroborated by their emission spectra (Figure S6 of the Supporting Information). Surprisingly, sensor 1 and sensor 2 retained 96 and 99% of their initial intensity at room temperature even after 30 days, respectively. However, sensor 3 retained 86% of its initial PL intensity measured at room temperature after a month. It is to be emphasized that there is no shift in the PL peak position for the three sensors, thus further indicating their high stability. The QD-nanofiber/Si shows the most degradation compared to thin-film and fiber configurations. Unlike thin-film and optical-fiber configurations where QDs are protected by PMMA encapsulation and built-in protection provided by the borosilicate cladding of the fiber, the QD-doped electrospun nanofibers have a sufficient number of QDs on the surface of nanofibers, which get easily degraded by the atmosphere, thus leading to a decrease in PL intensity with time.

4. CONCLUSIONS

This work reports the successful synthesis of highly emitting, nontoxic InP/ZnS core−shell QDs, which show temperature-dependent optical properties. The PL intensity decreases with an increasing temperature as a result of enhanced nonradiative recombination channels due to increased core−shell interfacial defect states and surface trap states, which can be explained by the Mott equation in the thermal quenching model. The QDs when heated show a slight redshift in the PL peak, which is due to the change in the energy band gap with temperature and explained well by Varshni's equation. The temperature-dependent absorption study reveals the attenuation of optical density and the redshift of the first exciton peak with an increased temperature. The study also demonstrates the feasibility of nontoxic InP/ZnS QD-PMMA nanocomposite-based temperature sensors, which have not been reported earlier. As-
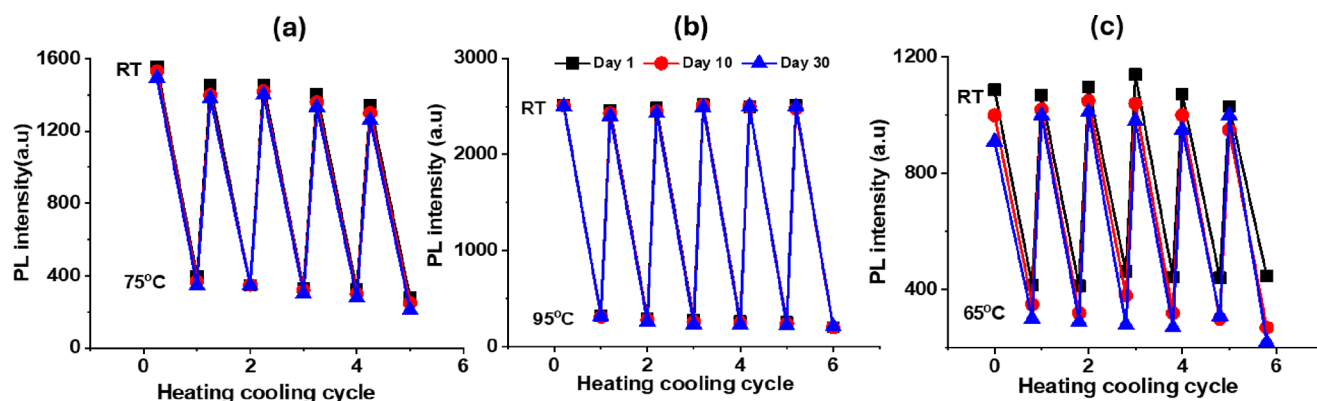
Figure 7. Heating−cooling cyclic reversibility measurement of PL intensity for day 1 (black), day 10 (red), and day 30 (blue) for (a) sensor 1 planar-configuration temperature sensor, (b) sensor 2 QD-PMMA-filled borosilicate fiber temperature sensor, and (c) sensor 3 QD-PMMA-doped electrospun nanofiber temperature sensor.

synthesized high-quality, nontoxic InP/ZnS QDs have been used to fabricate various configurations of temperature sensors such as the thin-film-based planar configuration, QD-filled optical fibers, and QD-doped electrospun nanofibers by making use of their temperature-dependent PL feature. The sensitivity of the sensors has been calculated, and it is found that the achieved sensitivity values are comparable to Cd-based temperature sensors reported to date. The temperature sensors exhibit excellent reversibility in a particular temperature range along with long-term stability and repeatability, which ensures a long service lifetime of the sensors under ambient conditions. It is expected that the strategy demonstrated in this work can be extended to the fabrication of other QD-based optical temperature sensors with a specific functionality. Thus, the synthesized InP/Zn-based QDs can be potential candidates to be used in various domains of nanothermometry and as promising replacement of toxic QD-based temperature sensors.

5. MATERIALS USED

Reagents were received in the following purities and used without further purification: 99.999% indium chloride (InCl$_3$) (Alfa Aesar), zinc chloride (ZnCl$_2$) (reagent-grade, ≥98%) (Sigma-Aldrich), 99.5% zinc oxide (ZnO) powder (extra pure AR, SRL), 99.99% sulfur (S) powder (Sigma-Aldrich), 97% tris(diethylamino)phosphine (P(DMA)$_3$), 90% trioctylphosphine technical grade (TOP) (Sigma-Aldrich), 90% 1-octadecene (ODE) technical grade (Sigma-Aldrich), 70% oleylamine (OLAm) technical grade (Sigma-Aldrich), oleic acid (OA) (extra pure, SRL), ethanol (Sigma-Aldrich), chloroform anhydrous, ≥99%, and poly(methyl methacrylate) (PMMA) (Sigma-Aldrich).

6. CHARACTERIZATION TOOLS USED

6.1. Transmission Electron Microscopy. The morphology of QDs was determined based on images collected using a transmission electron microscope TEM TITAN Themis (80−300 kV), operated at 300 kV (Field Electron and Ion Company). The samples were prepared by drop casting a diluted quantum dot solution on a copper TEM grid with lacey carbon films (400 mesh) and drying them completely.

6.2. XRD. X-ray diffraction (XRD) was performed using a Rigaku SmartLab X-ray diffractometer (operating voltage of 40 kV, current of 40 mA) with Cu Kα radiation ($\lambda = 1.5406$ Å) with a scanning range of 10−80° and a scanning rate of 3° min^{-1}.

6.3. UV−Vis Spectroscopy. UV−vis spectra were obtained using Hewlett Packard HP 8452A UV−vis diode array spectrophotometer. UV−vis spectra of the samples were obtained in quartz cuvettes (2 mL) with a 10 mm optical path at a scanning rate of 1.0 nm from 200 to 700 nm.

6.4. Fluorescence Spectroscopy. The fluorescence spectra were recorded using a SpectraMax i3x from Molecular Devices and FluoroMax Plus from Horiba Scientific under 350 nm excitation wavelength for 200 μL of the sample in quartz cuvettes (2 mL) with a 10 mm optical path length (scan speed of 20 nm min^{-1}, a slit width of 2 nm for excitation and emission).

6.5. Photoluminescence Quantum Yield (PLQY) Measurement. The absolute PLQY of the QDs was measured by a direct method using a Horiba FluoroMax Plus spectrofluorometer equipped with a Horiba QuantaPhi 2 PLQY integrating a sphere of 121 mm internal diameter. The excitation wavelength used was 350 nm, the excitation and emission slit width was 3 nm, and the integration time was 1 s. The formula used for PLQY (θ) calculation is given by eq 5.

$$\theta = \frac{E_c - (1 - A)\cdot E_b}{L_a \cdot A} = \frac{E_c - E_a}{L_a - L_c} \tag{5}$$

where E_c is the fluorescence emission, L_c is the scatter of the sample, E_a is the emission, L_a is the scatter of a blank, E_b is the integrated luminescence from the sample caused by indirect luminescence from the sphere, and A is the absorbance of the sample at the excitation wavelength.

6.6. Time-Resolved Fluorescence Lifetime Measurement. The temperature-dependent fluorescence lifetime was measured in a Horiba DeltaFlex modular TCSPC lifetime fluorometer with 350 nm excitation.

6.7. FTIR. The FTIR spectra were taken using an Analytik Jena SPECORD S 600 spectrophotometer, in the range of 400−4000 cm^{-1} at a resolution of 4 cm^{-1}; 16 scans were taken for each sample. The QDs had been mixed with dry KBr in an agate mortar, and a hydraulic press was used to press the mixture into a pellet under a 40 MPa pressure for 2 min in an evacuable slot.

6.8. Fluorescence Microscopy. The fluorescence microscopy images of the electrospun nanofibers were taken in an Olympus IX-71 fluorescence microscope with a xenon lamp and an excitation filter of 405 nm.

6.9. Optical Microscopy. Fibers during and after the electrospinning process were collected on a microscope slide for

optical analysis using an optical microscope (Olympus BX 53M).

6.10. SEM. A Zeiss Ultra 55 scanning electron microscope (SEM) was used to check the morphology and measure the diameters of the electrospun nanofibers.

ASSOCIATED CONTENT

Supporting Information

The Supporting Information is available free of charge at https://pubs.acs.org/doi/10.1021/acsomega.4c05644.

Schematic of the experimental setup of cyclic heating–cooling measurement, EDX analysis data of the InP/ZnS QDs, PLQY measurement data and detailed calculation, parameter to fit PL decay lifetime curves, QD-doped electrospun nano-/microfiber fabrication process and parameters in detail, schematic and optical image of formation of various droplets to electrospun nanofibers, and PL spectra taken on day 1 and day 30 for the three sensors (PDF)

AUTHOR INFORMATION

Corresponding Author

Asha Bhardwaj − *Instrumentation and Applied Physics Department, Indian Institute of Science, Bangalore 560012, India;* orcid.org/0000-0002-7839-2871; Email: asha@iisc.ac.in

Authors

Barnali Mahato − *Instrumentation and Applied Physics Department, Indian Institute of Science, Bangalore 560012, India*

Palash Kusum Das − *Instrumentation and Applied Physics Department, Indian Institute of Science, Bangalore 560012, India*

Complete contact information is available at:
https://pubs.acs.org/10.1021/acsomega.4c05644

Author Contributions

B.M. and P.K.D. contributed to this work equally. The manuscript was written through contributions of all authors. All authors have given approval to the final version of the manuscript.

Notes

The authors declare no competing financial interest.

REFERENCES

(1) García de Arquer, F. P.; Talapin, D. V.; Klimov, V. I.; Arakawa, Y.; Bayer, M.; Sargent, E. H. Semiconductor quantum dots: Technological progress and future challenges. *Science* **2021**, *373* (6555), No. eaaz8541.

(2) Martynenko, I. V.; Litvin, A. P.; Purcell-Milton, F.; Baranov, A. V.; Fedorov, A. V.; Gun'ko, Y. K. Application of semiconductor quantum dots in bioimaging and biosensing. *J. Mater. Chem. B* **2017**, *5*, 6701.

(3) Shang, C.; Wan, Y.; Selvidge, J.; Hughes, E.; Herrick, R.; Mukherjee, K.; Duan, J.; Grillot, F.; Chow, W. W.; Bowers, J. E. Perspectives on advances in quantum dot lasers and integration with Si photonic integrated circuits. *ACS Photonics* **2021**, *8*, 2555.

(4) Resch-Genger, U.; Grabolle, M.; Cavaliere-Jaricot, S.; Nitschke, R.; Nann, T. Quantum dots versus organic dyes as fluorescent labels. *Nature methods.* **2008**, *5*, 763−775.

(5) Brunetti, V.; Chibli, H.; Fiammengo, R.; Galeone, A.; Malvindi, M. A.; Vecchio, G.; Cingolani, R.; Nadeau, J. L.; Pompa, P. P. InP/ZnS as a safer alternative to CdSe/ZnS core/shell quantum dots: in vitro and in vivo toxicity assessment. *Nanoscale.* **2013**, *5*, 307−317.

(6) Xu, L.; Li, J.; Cai, B.; Song, J.; Zhang, F.; Fang, T.; Zeng, H. A bilateral interfacial passivation strategy promoting efficiency and stability of perovskite quantum dot light-emitting diodes. *Nat. Commun.* **2020**, *11* (1), 3902.

(7) Song, J.; Li, J.; Li, X.; Xu, L.; Dong, Y.; Zeng, H. Quantum dot light-emitting diodes based on inorganic perovskite cesium lead halides (CsPbX₃). *Advanced materials.* **2015**, *27* (44), 7162−7167.

(8) Xiong, L.; Qin, M.; Chen, C.; Wen, J.; Yang, G.; Guo, Y.; Ma, J.; Zhang, Q.; Qin, P.; Li, S.; Fang, G. Fully high-temperature-processed SnO2 as blocking layer and scaffold for efficient, stable, and hysteresis-free mesoporous perovskite solar cells. *Adv. Funct. Mater.* **2018**, *28* (10), 1706276.

(9) Liao, C.; Tang, L.; Li, Y.; Sun, S.; Wang, L.; Xu, J.; Jia, Y.; Gu, Z. Toward temperature-insensitive near-infrared optical gain using low-toxicity Ag 2 Se quantum dots. *Nanoscale.* **2022**, *14* (28), 10169−75.

(10) Wei, K.; Xu, Z.; Chen, R.; Zheng, X.; Cheng, X.; Jiang, T. Temperature-dependent excitonic photoluminescence excited by two-photon absorption in perovskite CsPbBr 3 quantum dots. *Optics letters.* **2016**, *41* (16), 3821−4.

(11) Jing, P.; Zheng, J.; Ikezawa, M.; Liu, X.; Lv, S.; Kong, X.; Zhao, J.; Masumoto, Y. Temperature-dependent photoluminescence of CdSe-core CdS/CdZnS/ZnS-multishell quantum dots. *J. Phys. Chem. C* **2009**, *113* (31), 13545−50.

(12) Morello, G.; De Giorgi, M.; Kudera, S.; Manna, L.; Cingolani, R.; Anni, M. Temperature and size dependence of nonradiative relaxation and exciton− phonon coupling in colloidal CdTe quantum dots. *J. Phys. Chem. C* **2007**, *111* (16), 5846−9.

(13) Al Salman, A.; Tortschanoff, A.; Mohamed, M. B.; Tonti, D.; Van Mourik, F.; Chergui, M. Temperature effects on the spectral properties of colloidal CdSe nanodots, nanorods, and tetrapods. *Appl. Phys. Lett.* **2007**, *90*, No. 093104.

(14) Allison, S. W.; Gillies, G. T. Remote thermometry with thermographic phosphors: Instrumentation and applications. *Review of scientific instruments.* **1997**, *68*, 2615−2650.

(15) Yan, D.; Lu, J.; Ma, J.; Wei, M.; Evans, D. G.; Duan, X. Reversibly thermochromic, fluorescent ultrathin films with a supramolecular architecture. *Angew. Chem., Int. Ed.* **2011**, *50*, 720−723.

(16) Maruszewski, K.; Andrzejewski, D.; Strek, W. Thermal sensor based on luminescence of Ru (bpy) 32+ entrapped in sol-gel glasses. *Journal of luminescence.* **1997**, *72−74*, 226−228.

(17) Walker, G. W.; Sundar, V. C.; Rudzinski, C. M.; Wun, A. W.; Bawendi, M. G.; Nocera, D. G. Quantum-dot optical temperature probes. *Appl. Phys. Lett.* **2003**, *83*, 3555−3557.

(18) Bueno, A.; Suarez, I.; Abargues, R.; Sales, S.; Pastor, J. P. Temperature sensor based on colloidal quantum dots−PMMA nanocomposite waveguides. *IEEE sensors journal.* **2012**, *12*, 3069−3074.

(19) Joshi, A.; Narsingi, K. Y.; Manasreh, M. O.; Davis, E. A.; Weaver, B. D. Temperature dependence of the band gap of colloidal CdSe/ ZnS core/shell nanocrystals embedded into an ultraviolet curable resin. *Appl. Phys. Lett.* **2006**, *89*, 131907.

(20) Li, S.; Zhang, K.; Yang, J. M.; Lin, L.; Yang, H. Single quantum dots as local temperature markers. *Nano letters.* **2007**, *7*, 3102−3105.

(21) Narayanaswamy, A.; Feiner, L. F.; Van Der Zaag, P. J. Temperature dependence of the photoluminescence of InP/ZnS quantum dots. *J. Phys. Chem. C* **2008**, *112*, 6775−6780.

(22) Narayanaswamy, A.; Feiner, L. F.; Meijerink, A.; Van der Zaag, P. J. The effect of temperature and dot size on the spectral properties of colloidal InP/ZnS core− shell quantum dots. *ACS Nano* **2009**, *3*, 2539−2546.

(23) Rowland, C. E.; Liu, W.; Hannah, D. C.; Chan, M. K.; Talapin, D. V.; Schaller, R. D. Thermal stability of colloidal InP nanocrystals: small inorganic ligands boost high-temperature photoluminescence. *ACS Nano* **2014**, *8*, 977−985.

(24) Shirazi, R.; Kopylov, O.; Kovács, A.; Kardynał, B. E. Temperature dependent recombination dynamics in InP/ZnS colloidal nanocrystals. *Appl. Phys. Lett.* **2012**, *101*, No. 091910.

(25) Savchenko, S. S.; Vokhmintsev, A. S.; Weinstein, I. A. Photoluminescence thermal quenching of yellow-emitting InP/ZnS quantum dots. *AIP Conf. Proc.* **2018**, *2015*, No. 020085.

(26) Biadala, L.; Siebers, B.; Beyazit, Y.; Tessier, M. D.; Dupont, D.; Hens, Z.; Yakovlev, D. R.; Bayer, M. Band-edge exciton fine structure and recombination dynamics in InP/ZnS colloidal nanocrystals. *ACS Nano* **2016**, *10*, 3356−3364.

(27) Wang, C.; Wang, Q.; Zhou, Z.; Wu, W.; Chai, Z.; Gao, Y.; Kong, D. Temperature dependence of photoluminescence properties in InP/ZnS core-shell quantum dots. *J. Lumin.* **2020**, *225*, No. 117354.

(28) Mahato, B; Das, P. K.; Bhardwaj, A. InP/ZnS core shell quantum dots as temperature sensor. In *2022 IEEE International Conference on Emerging Electronics (ICEE) 2022*; IEEE: 2022 .

(29) Tang, L.; Zhang, Y.; Liao, C.; Guo, Y.; Lu, Y.; Xia, Y.; Liu, Y. Temperature-dependent photoluminescence of CdS/ZnS core/shell quantum dots for temperature sensors. *Sensors.* **2022**, *22*, 8993.

(30) Zhou, Y.; Buhro, W. E. Reversible exchange of L-type and bound-ion-pair X-type ligation on cadmium selenide quantum belts. *J. Am. Chem. Soc.* **2017**, *139*, 12887−12890.

(31) Leroux, M.; Grandjean, N.; Beaumont, B.; Nataf, G.; Semond, F.; Massies, J.; Gibart, P. Temperature quenching of photoluminescence intensities in undoped and doped GaN. *J. Appl. Phys.* **1999**, *86*, 3721−3728.

(32) Reshchikov, M. A. Mechanisms of thermal quenching of defect-related luminescence in semiconductors. *Phys. Status Solidi A* **2021**, *218*, 2000101.

(33) Nikiforov, S. V.; Kortov, V. S.; Savushkin, D. L.; Vokhmintsev, A. S.; Weinstein, I. A. Thermal quenching of luminescence in nano-structured monoclinic zirconium dioxide. *Radiat. Meas.* **2017**, *106*, 155−160.

(34) Savchenko, S. S.; Vokhmintsev, A. S.; Weinstein, I. A. Temperature-induced shift of the exciton absorption band in InP/ZnS quantum dots. *Optical Materials Express.* **2017**, *7*, 354−359.

(35) Savchenko, S. S.; Weinstein, I. A. Inhomogeneous broadening of the exciton band in optical absorption spectra of InP/ZnS nanocrystals. *Nanomaterials.* **2019**, *9*, 716.

(36) Li, B.; Liu, W.; Yan, L.; Zhu, X.; Yang, Y.; Yang, Q. Revealing mechanisms of PL properties at high and low temperature regimes in CdSe/ZnS core/shell quantum dots. *J. Appl. Phys.* **2018**, *124*, No. 044302.

(37) Gaponenko, M. S.; Lutich, A. A.; Tolstik, N. A.; Onushchenko, A. A.; Malyarevich, A. M.; Petrov, E. P.; Yumashev, K. V. Temperature-dependent photoluminescence of PbS quantum dots in glass: Evidence of exciton state splitting and carrier trapping. *Phys. Rev. B* **2010**, *82*, No. 125320.

(38) Lee, H.; Yang, W.; Sercel, P. C. Temperature and excitation dependence of photoluminescence line shapein InAs/GaAs quantum-dot structures. *Phys. Rev. B* **1997**, *55*, 9757.

(39) Le Ru, E. C.; Fack, J.; Murray, R. Temperature and excitation density dependence of the photoluminescence from annealed InAs/GaAs quantum dots. *Phys. Rev. B* **2003**, *67*, No. 245318.

(40) Lobo, C.; Leon, R.; Marcinkevicius, S.; Yang, W.; Sercel, P. C.; Liao, X. Z.; Zou, J.; Cockayne, D. J. Inhibited carrier transfer in ensembles of isolated quantum dots. *Phys. Rev. B* **1999**, *60*, 16647.

(41) Espiau de Lamaëstre, R.; Bernas, H.; Pacifici, D.; Franzó, G.; Priolo, F. Evidence for a "dark exciton" state of PbS nanocrystals in a silicate glass. *Appl. Phys. Lett.* **2006**, *88*, 181115.

(42) Labeau, O.; Tamarat, P.; Lounis, B. Temperature dependence of the luminescence lifetime of single C d S e/Z n S quantum dots. *Phys. Rev. Lett.* **2003**, *90*, No. 257404.

(43) Eilers, J.; Van Hest, J.; Meijerink, A.; Donega, C. D. Unravelling the size and temperature dependence of exciton lifetimes in colloidal ZnSe quantum dots. *J. Phys. Chem. C* **2014**, *118*, 23313−23319.

(44) De Mello Donegá, C.; Bode, M.; Meijerink, A. Size-and temperature-dependence of exciton lifetimes in CdSe quantum dots. *Phys. Rev. B* **2006**, *74*, No. 085320.

(45) Kalytchuk, S.; Zhovtiuk, O.; Kershaw, S. V.; Zbořil, R.; Rogach, A. L. Temperature-dependent exciton and trap-related photolumines-cence of CdTe quantum dots embedded in a NaCl matrix: implication in thermometry. *Small.* **2016**, *12*, 466−476.

(46) Liang, R.; Tian, R.; Shi, W.; Liu, Z.; Yan, D.; Wei, M.; Evans, D. G.; Duan, X. A temperature sensor based on CdTe quantum dots−layered double hydroxide ultrathin films via layer-by-layer assembly. *Chemical communications.* **2013**, *49*, 969−971.

(47) Hajduk, B.; Bednarski, H.; Jarka, P.; Janeczek, H.; Godzierz, M.; Tański, T. Thermal and optical properties of PMMA films reinforced with Nb2O5 nanoparticles. *Sci. Rep.* **2021**, *11* (1), 22531.

(48) Meng, C.; Xiao, Y.; Wang, P.; Zhang, L.; Liu, Y.; Tong, L. Quantum-dot-doped polymer nanofibers for optical sensing. *Adv. Mater.* **2011**, *23*, 3770−3774.

(49) Chen, Y.; Rosenzweig, Z. Luminescent CdS quantum dots as selective ion probes. *Anal. Chem.* **2002**, *74*, 5132−5138.

(50) Nazzal, A. Y.; Qu, L.; Peng, X.; Xiao, M. Photoactivated CdSe nanocrystals as nanosensors for gases. *Nano letters.* **2003**, *3*, 819−822.

(51) Ennis, D.; Golden, D.; Curtin, M. C.; Cooper, A.; Sun, C.; Riegner, K.; Johnson, C. C.; Nolletti, J. L.; Wallace, K. B.; Chacon, J. A.; Bethune, H.; Ritchie, T. S.; Schnee, V.; DeNeve, D. R.; Riegner, D. E. Quantum Dot-Doped Electrospun Polymer Fibers for Explosive Vapor Sensors. *ACS Appl. Nano Mater.* **2023**, *6*, 9315−9321.

(52) Brites, C. D.; Lima, P. P.; Silva, N. J.; Millán, A.; Amaral, V. S.; Palacio, F.; Carlos, L. D. *Thermometry at the nanoscale. Nanoscale.* **2012**, *4*, 4799−4829.

(53) Wang, X. D.; Wolfbeis, O. S.; Meier, R. J. Luminescent probes and sensors for temperature. *Chemical Society Reviews.* **2013**, *42*, 7834−7869.